Steven Marczak
Elaine Smith
Satyajyoti Senapati (iD)
Hsueh-Chia Chang (iD)

Department of Chemical and
Biomolecular Engineering,
University of Notre Dame, Notre
Dame, IN, USA

Research Article

Selectivity enhancements in gel-based DNA-nanoparticle assays by membrane-induced isotachophoresis: thermodynamics versus kinetics

Selectivity against mutant nontargets with a few mismatches remains challenging in nucleic acid sensing. Sensitivity enhancement by analyte concentration does not improve selectivity because it affects targets and nontargets equally. Hydrodynamic or electrical shear enhanced selectivity is often accompanied by substantial losses in target signals, thereby leading to poor limits of detection. We introduce a platform based on depletion isotachophoresis in agarose gel generated by an ion-selective membrane that allows both selectivity and sensitivity enhancement with a two-step assay involving concentration polarization at an ion-selective membrane. By concentrating both the targets and probe-functionalized nanoparticles by ion enrichment at the membrane, the effective thermodynamic dissociation constant is lowered from 40 nM to below 500 pM, and the detection limit is 10 pM as reported previously. A dynamically optimized ion depletion front is then generated from the membrane with a high electrical shear force to selectively and irreversibly dehybridize nontargets. The optimized selectivity against a two-mismatch nontarget (in a 35-base pairing sequence) is shown to be better than the thermodynamic equilibrium selectivity by more than a hundred-fold, such that there is no detectable signal from the two-mismatch nontarget. We offer empirical evidence that irreversible cooperative dehybridization plays an important role in this kinetic selectivity enhancement and that mismatch location controls the optimum selectivity even when there is little change in the corresponding thermodynamic dissociation constant.

1 Introduction

Research into the profiling of microRNA (miRNA), circulating tumor DNA (ctDNA), and messenger RNA (mRNA) has suggested accurate quantification of their expression levels may prove to be a valid method of diagnosing various diseases, disorders, and cancers. They may also potentially be used to measure the efficacy of different therapeutic treatments to discern which has the most promising outcome for a particular patient [1–4]. These informative biomarkers are short nucleic acids ranging from about 19–26 nucleotides for miRNA, 50–200 bases for ctDNA, and up to 1000 bases for mRNA. Standard genomic biopsy detection and quantification techniques in use today suffer from the need for large, expensive equipment, highly skilled lab personnel, long assay times, and time-consuming pretreatment. While the gold standard technique, reverse transcriptase polymerase chain reaction (RT-PCR), possesses the desirable characteristics of large dynamic range, sequence-specific amplification, and low limits of detection, it does not actually quantify the concentration of RNA but rather determines the number of cycles required for specific amplification [5, 6]. Thus, relative measures such as cycle of quantitation are reported instead of concentrations. A second challenge faced by nucleic acid sensors is low concentration of the target nucleic acid. In the case of miRNA, they account for as little as 0.01% of the total mass of RNA from a cell [7]. Although a considerable amount of nucleic acids may be extracted from dissected or fresh tissue, these methods are invasive and pose significantly higher risks to patients. The more desirable approach, detecting nucleic acids through liquid biopsies, yields quantities two to three orders of magnitude lower [8]. Sample purification also introduces a number of opportunities for sample loss. For example, Qu et al. reported a method to simultaneously separate proteins and DNA by solution isotachophoresis, yet they noted DNA–protein interactions and nonspecific adsorption

Correspondence: Professor Hsueh-Chia Chang, Department of Chemical and Biomolecular Engineering, University of Notre Dame, 182 Fitzpatrick Hall, Notre Dame Avenue, Notre Dame, IN 46556, USA
E-mail: hchang@nd.edu

to the walls of the microfluidic channel led to some loss of the DNA sample [9]. Likewise, in other purification protocols [10], a substantial portion of the sample may be lost before it is ready to be assayed. Although pushing the limits of detection even lower is one solution, reducing the number of purification steps is highly desirable.

One method of addressing the issue of low starting material is employing preconcentration techniques which concentrate the sample of interest into the detection zone. These techniques are particularly important because in many instances DNA probes are functionalized onto a surface, and their dissociation constants are relatively low compared to hybridization pairs floating in solution. For example, the dissociation constants are typically on the order of 1–10 μM for hybridization to DNA probes functionalized to gold nanoparticles [11], 1–10 nM for probes functionalized to gold films [12], and less than pM for probes in solution [11, 13]. The hybridization to probe-functionalized nanoparticles may be improved by various means such as adjusting particle size [14, 15], inserting nucleotide spacers between the particles and pairing sequences [1, 14–16], increasing the length of the probe [11, 13], optimizing the probe density [14–16], and adjusting the solution's ionic strength [14, 15].

Another way to overcome the barrier imposed by these relatively high dissociation constants is through preconcentration of the sample, the nanoparticles, or both with the ion-selective features of nanofluidic channels. Han's group extensively studied preconcentration using nanofluidic junctions in microfluidic channels [17–20]. Quist et al. used isotachophoresis of the depletion front from a nanochannel to not only concentrate their sample in a flowing solution but also to separate fluorescent analytes as well in the microchannel [21, 22]. The ion selectivity feature of the nanochannel produces a depletion zone that allows them to achieve such concentration and separation.

We recently advanced the use of ion-selective membranes in place of nanofluidic channels to achieve both ion depletion and enrichment [23]. We used the ion-selective membrane to preconcentrate probe-functionalized nanoparticles and the target molecules with ion enrichment against the membrane without flow [24]. We then separate the target-linked dimer particles from the unlinked monomer particles with an ion depletion front away from the membrane. Our assay involved two steps that utilize both the concentration enrichment and depletion actions of an ion-selective membrane sequentially. It also utilized gel to suppress electroosmotic flow in the microchannel, which tends to reduce the enrichment and depletion factors. We used microchannels fabricated from polycarbonate for the same reason. The result is a two orders of magnitude concentration factor and roughly the same enhancement in sensitivity due to the preconcentration by enrichment. Because of the absence of electroosmotic flow, a robust depletion front that can advance the length of the gel-filled microchannel was also observed. The isotachophoretic or packing action of this strong depletion front allows separation of unlinked nanoparticles (or nanoparticles linked by nontargets).

However, the selectivity issue was not scrutinized in our early work [24]. This is important as enhanced sensitivity often comes at a cost of reduced selectivity. In nucleic acid sensing, selectivity describes the ability to discriminate between similar DNA sequences. In practical terms, it is the capacity of a sensor probe sequence to distinguish its complementary target sequence from nontarget sequences that possess as little as one or two mismatches. For instance, de Avila et al., using square-wave voltammetry, found it difficult to discriminate between targets and nontargets with only one-base mismatches when the number of bases in the pairing sequence rose above thirteen [25]. This introduces serious complications for platforms even as robust as RT-PCR. In fact, this type of complication is especially serious for RT-PCR due to the widely varying melting temperatures of difference sequences caused by variable GC content. This leads to amplification biases which severely undermines accurate quantification [7, 8, 26]. Bias introduced by variable GC content also poses a problem for microarrays which rely on stringent temperature washes to ensure sufficient selectivity. For miRNAs, ligation bias significantly hinders their accurate quantification by PCR [27]. Other types of biosensors attempting to address these issues have seen limited progress. Sedighi et al. used targets conjugated to Au nanoparticles to achieve selectivity values of three to six for one-base mismatches [28] while Cao et al. reported selectivity values of two to three for an assay based on molecular beacons and silver nanoclusters [29]. However, while these articles report selectivity values, they failed to report what extent their technique, if at all, improved over the free solution thermodynamic limit of selectivity [29–35]. Hence, it is unclear if the reported selectivity represents an improvement attributable to assay design or if it simply a natural feature of the chemical thermodynamics.

While preconcentration may increase hybridization rates and lower limits of detection for microfluidic assays, many of them still do not possess any built-in mechanism to deal with the issue of selectivity. For example, Garcia-Schwarz and Santiago [36] and Bercovici et al. [37] demonstrated they could utilize the preconcentration feature of isotachophoresis with two immiscible buffers to enhance hybridization reaction rates between molecular beacons and their targets and rapidly achieve detection limits on the order of pM. However, these techniques did not selectively concentrate only the target molecules but rather all molecules. Thus, enhanced hybridization rates leading to lower limits of detection for target molecules will also result in lower limits of detection for nontarget molecules which becomes problematic when dealing with nucleic acid targets with only one or two mismatches. This can be especially troublesome when dealing with longer pairing sequences [25].

Applying shear forces through hydrodynamic flow or electric fields, though, may enhance the selectivity. For instance, Sosnowski et al., after hybridizing 19-mer and 22-mer targets to oligonucleotide probes functionalized onto a platinum electrode array, deployed electric fields to dehybridize

nontargets with single base-pair mismatches [38]. Cheng et al. used dielectrophoresis to concentrate DNA targets in a nanocolloid assembly and enhance hybridization while simultaneously using hydrodynamic shear to ensure selectivity between targets and nontargets with a single base-pair mismatch [39]. Cheng et al. further developed this technique to accurately quantify and discriminate between different species of *Candida* cells [40]. A long, unpaired portion of the sequence allowed them to generate a significant electric force due to the charged phosphate backbone. This required DNA sizes on the order of kilobases, so it is unclear if their technique is applicable to short nucleic acids. Even so, substantial loss in signal often accompanies the selectivity enhancement thereby raising the limit of detection [38–42]. Therefore, a new technique which enables the selective discrimination of nucleic acids with similar sequences while maintaining the signal from the target is needed.

As a step in this direction, we expand upon our previous work on field-induced aggregation of gold nanoparticles with captured DNA targets by enhancing selectivity with depletion isotachophoresis [24]. In our recently developed technique, we exploited the effects of both ion enrichment and depletion at the interface of a nanoporous, ion-selective membrane and a microfluidic channel. Slouka et al. describes the mechanisms behind these phenomena in a recent review [23]. In our assay, we switch the electric field direction after the enrichment step that concentrates the analytes and nanoparticles at the membrane in order to produce a depletion front. An ion-depleted zone with high electric field and shear then grows from the membrane. We use this high shear rate to break up nanoparticles linked by nontargets and selectively remove them by the depletion front, as they are isotachophoretically packed against the depletion front with a higher trailing field and a lower preceding field. Because both the linked and unlinked particles initially migrate at the same speed in an electrical conductivity gradient created by the propagation of the depletion zone prior to induced aggregation of the linked particles, we termed our technique depletion isotachophoresis. We evaluate the remaining linked nanoparticles based on the optical properties of gold nanoparticles to quantify the number of target DNAs.

We presented preliminary results illustrating the effect of ramping the electric field during the depletion step. This step of our assay is critical for maximizing the selectivity of DNA sequences closely resembling each other. Here, we elaborate on the efficacy of our new assay by examining the effects of altering electric field strengths and their duration as well as the effects of nucleotide mismatch location and number. We base our design on the cooperative melting mechanism of DNA from gold nanoparticles described in previous literature [14, 43, 44]. Cooperativity describes how targets already hybridized to nanoparticle probes influence the ability for further hybridization by subsequent DNA targets. Negative cooperativity indicates further hybridization will be more difficult whereas positive cooperativity indicates further hybridization is energetically more favorable. Lei et al. extensively characterized the intermolecular interactions determining whether

cooperativity is positive, negative, or neutral [43]. While electrostatic forces play a major role as demonstrated by Jin et al. [14] and Lytton-Jean et al. [44], orientational interactions, hydration repulsion, and excluded volume also play significant roles [43]. Under the proper conditions, cooperativity can be used to improve selectivity and achieve single-base pair mismatch discrimination. We apply our technique to take advantage of this phenomenon and maximize the selectivity of our assay. Although there is a natural tradeoff between signal intensity and selectivity, cooperative melting improves this tradeoff. By ramping the strength of the electric field during our depletion step, we significantly improve the selectivity while at the same time minimizing the loss of signal intensity provided by the plasmonic gold nanoparticles. The electric field also provides a means to make the dehybridization irreversible so as to prevent the nanoparticles from recapturing nontargets and reducing the selectivity. In addition, we critically compare the dissociation constants and selectivity of our assay to values achieved by the same probes and targets in bulk solution to validate the enhanced selectivity. Despite the adjustments to our previous protocol to optimize selectivity, we maintain short assay times and low limits of detection.

2　Materials and methods

2.1　Materials

Gold nanoparticles with mean diameter 20 nm were provided by nanoComposix, Inc. Sodium chloride was obtained from Sigma-Aldrich. SYBR green I was received at 10 000× concentration from Invitrogen. Buffers were prepared by dilution from 10× PBS (pH 7.4) and 50× TAE (pH 8.4) from Boston Bioproducts, 1× TE (pH 8.0) from Integrated DNA Technologies, Inc., and 150 mM sodium phosphate buffer (pH 7.2) from Teknova. Agarose gels were prepared at 1 wt% in 1× TAE using agarose powder from Ominpur and stored as liquids inside an oven maintained at 65°C. Quik-Cast polyurethane casting resins (side A and side B) were obtained from TAP Plastics Inc. Acrifix 1R 0192 UV reactive cement was obtained from Evonik Industries while Loctite 3492 light cure adhesive was obtained from Loctite Corporation. Custom single-stranded DNA probes and target sequences were provided by Integrated DNA Technologies Inc., and the sequences are listed in Table 1. Probe 1 possessed a thiol modification at the 5' terminus while probe 2 possessed a thiol modification at the 3' terminus. The probes were prepared for use by dissolution at 0.1 mM in a 1 × TE buffer containing 10 mM DL-dithiothreitol (DTT). The DTT, obtained as a solid from BioWorld, was used to reduce the thiol modifiers from their oxidized form by reacting at room temperature for two hours. After the reaction was complete, the solution was purified from the DTT by running it through a Roche mini Quick Spin DNA column. Concentrations were determined from absorbance measurements on a Thermo Scientific NanoDrop2000 spectrophotometer using the 260 nm peak. Although it is possible to functionalize

Table 1. DNA sequences

Name	Label	Sequence (5′→3′)
Probe 1	P1	TGG TTC TCT CCG AAA TAG CTT TAG GGC TA
Probe 2	P2	GAA GGG AAG AGG AAG AGG CAG GTG TCC TGT GGT AG
Perfect target	PT	CT ACC ACA GGA CAC CTG CCT CTT CCT CTT CCC TTC AAAAA TA GCC CTA AAG CTA TTT CGG AGA GAA CCA
Mismatch2a	MM2a	CT ACC **GTA** GGA CAC CTG CCT CTT CCT CTT CCC TTC AAAAA TA GCC CTA AAG CTA TTT CGG AG**G** **CAA** CCA
Mismatch2b	MM2b	CT ACC ACA GGA CAC CTG CCT CTT CCT CTT CCC T**AT** AAAAA **AG** GCC CTA AAG CTA T**TT** CGG AGA GAA CCA
Mismatch4a	MM4a	CTA **TTG** TAG GAC ACC TGC CTC TTC CTC TTC CCT TC AAAAA TA GCC CTA AAG CTA TTT CGG AG**G** **CGG** CCA
Mismatch4b	MM4b	CT ACC ACA GGA CAC CTG CCT CTT CCT CTT CCT **AAT** AAAAA **AG** TTC CTA AAG CTA TTT CGG AGA GAA CCA

P1 and P2 possessed dithiol modifiers at the 5′ and 3′ termini, respectively. Bold letters are bases not part of pairing sequence. Underlined bases are mismatches.

DNA onto gold nanoparticles without DTT reduction and spin column purification, we found these two steps to be critical to improving the performance of our assay in terms of selectivity. The DNA targets/mismatches were dissolved in 1× TE buffer at concentrations of 0.1 mM. All DNA was stored in the freezer at −20°C until ready for use. RALEX cation-exchange membranes whose fixed negative charge is supplied by organosulfanate groups were provided by Mega a.s (Czech Republic).

2.2 Determination of thermodynamic dissociation constants

Nanoparticles were functionalized with DNA probes following the method of Hill et al. [16]. Typically, after reduction by DTT and purification by spin column, probe P1 was added to 500 μL of a 1 nM nanoparticle solution and incubated at 4°C for at least 12 h. Subsequently, 100 mM phosphate buffer was added to the solution to a final concentration of 10 mM. Then 2 M NaCl was added to final concentrations of 0.04, 0.09, 0.15, and 0.30 M in 1-h increments. After incubating at 4°C for another twelve hours, the functionalized particles were washed twice with 500 μL 0.1× PBS using centrifugation speeds of 13 000 rpm for 25–30 min before finally being redispersed in 50 μL 0.1× PBS. The nanoparticle concentration was adjusted to 5 nM by dilution with 0.1× PBS and

stored at 4°C until ready for use. An identical procedure was used for probe P2.

Nanoparticle concentrations were determined by a Tecan Infinite M200 Pro spectrophotometer. For melting curve experiments, a 1 nM: 1 nM mixture of nanoparticles with probes P1 and nanoparticles with probes P2 was used in 1 × TAE buffer. Target DNA sequences PT, MM2a, MM2b, MM4a, and MM4b were added to separate solutions at concentrations of 2, 4, 6, and 8 μM and allowed to mix for 48 h. After mixing, SYBR green I was added to a concentration of 2× and allowed to react for 1 h. Melting curves were collected using a Quantagene q225 from Beijing Coolight Technologies. The temperature was raised from 20 to 55°C in increments of 1°C. Each temperature was held for two minutes and fluorescent measurements were recorded every 20 s. Five replicates of each target sequence at each concentration were performed.

2.3 Chip fabrication

Microfluidic chips were fabricated in the same fashion as our previous work [24] from 300 μM polycarbonate sheets in a layer-by-layer fashion. There were four channels, 2 mm width × 15 mm length × 500 μM height which intersected in the center of the chip. Fluid inlets were set at the ends of the channel. Each channel was bisected by a 10 mm long cross-channel for the sample inlet. A 6.9 mm diameter hole was placed in the center of the chip to hold the membrane cast. A 4 mm × 4 mm cation-exchange membrane was sealed to the bottom of the cast and remained flush with the top of the microfluidic channel. The chip is shown in Fig. 1.

2.4 Selectivity studies

Chips were filled with agarose gel and used after the gel solidified. The gel was removed from the intersection, and then the cross-channel was filled with buffer until ready for use. The sample mixture contained a 5 nM: 5 nM ratio of nanoparticles functionalized with P1 and nanoparticles functionalized with P2 and 10 nM DNA which were mixed immediately prior to use. The buffer was removed from the cross-channel and the sample inserted in its place (Fig. 1A). The fluid reservoirs were all filled with 1× TAE buffer. Gel electrophoresis was conducted using a Keithley 2400A Sourcemeter with platinum electrodes as the voltage source initially located in the membrane reservoir and the gel inlet reservoir. The protocol consisted of two important steps: enrichment, where the particles pack against the membrane, and depletion, where the field is reversed and a region depleted of ions grows from the membrane toward the inlet reservoir. During the enrichment step, as seen in Fig. 1B, a positive electrode above the membrane electrophoretically drives the particles towards the membrane using a 110 V potential for 6 min. During depletion, Fig. 1C, the electrode in the membrane reservoir is
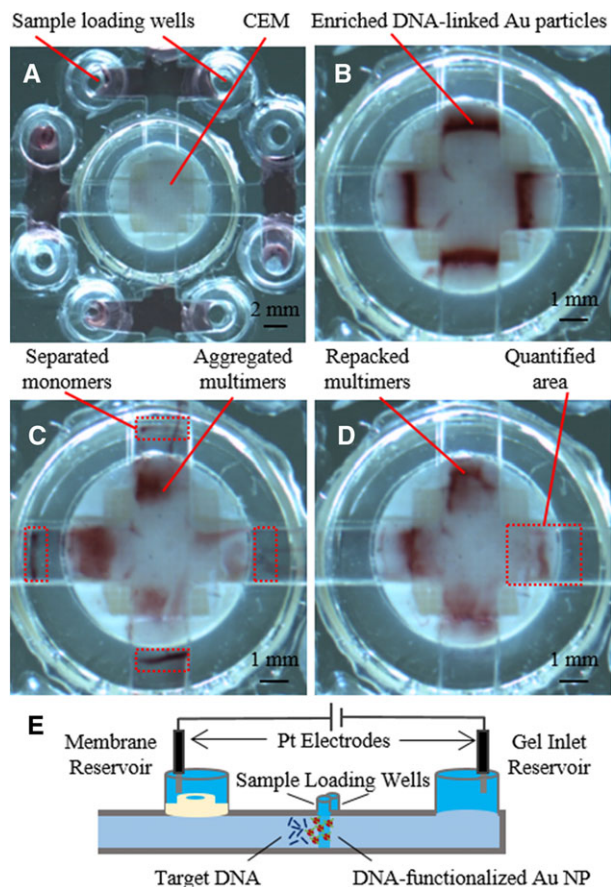
Sample loading wells   CEM   Enriched DNA-linked Au particles

Separated monomers   Aggregated multimers   Repacked multimers   Quantified area

E   Membrane Reservoir   Pt Electrodes   Gel Inlet Reservoir   Sample Loading Wells   Target DNA   DNA-functionalized Au NP

Figure 1. View from below chip. All images are taken with the same sample. (A) Sample is loaded into cross-channel. (B) Enrichment drives particles towards membrane. (C) Depletion separates monomers from aggregate possessing target. (D) Particles are repacked at membrane for quantification. (E) Profile view of one channel. The three remaining channels intersect at the membrane and have identical electrode placement. CEM stands for cation-exchange membrane.

changed to a negative potential. The magnitude and duration of the depletion potential was varied in order to study its capacity for enhancing the selectivity between targets and nontargets. The potential was initiated at −200 V for various times and then lowered to −125 V until the migrating particles reached the intersection. The particles were removed by vacuum and the cross-channel fluid was replaced with $1 \times$ TAE. The potential was changed to 150 V for 20–30 s to repack the aggregated particles against the membrane (Fig. 1D).

The nanoparticles were imaged using a QImaging Retiga 2000R Fast 1394 camera, an exposure time of 0.1 s, and custom MATLAB programming. Three images of the chip were recorded: one prior to the start of the experiment (initial image), one after the enrichment (enrichment image), and one after repacking the particles against the membrane (repacking image). After converting the images to grayscale, the nanoparticle signal was isolated in the enrichment and repacking images by subtracting the

initial image from them. The particles near the membrane were quantified using ImageJ. The area near the membrane was selected (Fig. 1D), a threshold was set to eliminate noise, and then the mean pixel intensity was determined using the measure function in ImageJ. The fraction of aggregated particles was then calculated by taking the ratio of the intensity after repacking to the intensity after enrichment.

3 Results

We obtained thermodynamic dissociation constants for the hybridization of different DNA sequences to probe-functionalized gold nanoparticles in a solution-based assay by recording melting curves at numerous target and mismatch concentrations. The melting temperature, T_M, occurs at the inflection point on the melting curve (Fig. 2A). We determined this point by taking the derivative of the data numerically using the central finite difference method and then recording the maximum (Fig. 2B). From the melting curves, we plotted the melting temperatures versus the concentrations, C. We determined the enthalpies and entropies of hybridization, ΔH_{hyb} and ΔS_{hyb}, respectively, from the slope
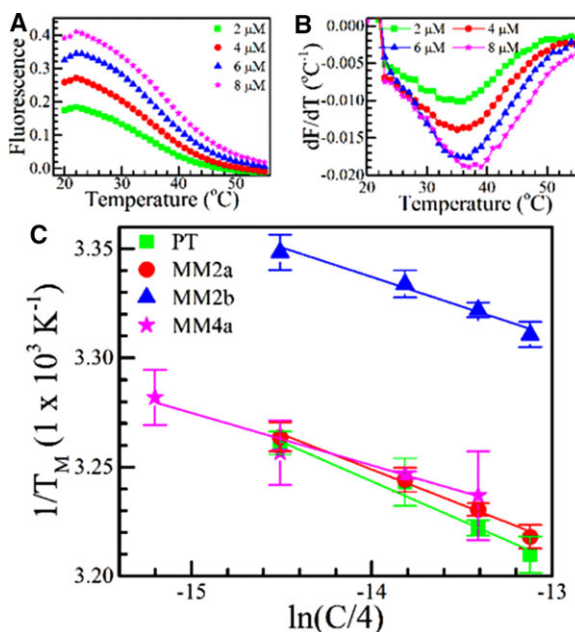

Figure 2. (A) Representative melting curves for the various concentrations of target, PT. Fluorescence intensity is in arbitrary units. (B) Corresponding first derivatives of the melting curves in (A) where F is fluorescence intensity and T is temperature. (C) Enthalpies and entropies of hybridization were derived from melting temperatures at different concentrations according to Eq. (1). Coefficients of determination for linear fits are 0.97, 0.99, 0.98, and 0.96 for target, mismatch2a, mismatch2b, and mismatch4a, respectively. Error bars are uncertainties within 95% confidence intervals and sample size $n = 5$.

Table 2. Dissociation constants

Sequence	ΔS_{hyb} (kJ/mol)	ΔH_{hyb} (kJ/mol)	ΔG_{hyb} (kJ/mol)	K_D (nM)
PT	-0.61 ± 0.08	-223 ± 26	-42 ± 1	42 ± 24
MM2a	-0.72 ± 0.05	-256 ± 17	-43 ± 1	30 ± 14
MM2b	-0.93 ± 0.09	-312 ± 31	-36 ± 2	400 ± 250
MM4a	-1.34 ± 0.08	-443 ± 28	-42 ± 4	42 ± 59

and y-intercept of the lines of best fit in Fig. 2C according to Eq. (1) where R is the gas constant [45].

$$\frac{1}{T_M} = \frac{R}{\Delta H_{hyb}} \ln\left(\frac{C}{4}\right) - \frac{\Delta S_{hyb}}{\Delta H_{hyb}} \tag{1}$$

The MM4b sequence is not shown because the melting temperatures were too low. We then determined the free energies of the hybridization reactions, ΔG_{hyb}, at 298 K and then calculated the dissociation constants, K_D, presented in Table 2 by using Eq. (2):

$$\frac{1}{K_D} = e^{-\Delta G_{hyb}/RT} \tag{2}$$

The dissociation constants are on the order of 50 nM and are consistent with previously reported results for similar systems [11, 13]. Lower dissociation constants indicate superior sensitivity because probes more readily hybridize with targets at lower concentrations. In this system, however, order of 10 nM dissociation constants are relatively high compared to the relevant samples of interest where the concentrations of DNA or RNA biomarkers are typically on the order of pM or lower. From Table 2, it is also clear that a solution-based equilibrium assay provides poor selectivity. For an equilibrium assay, the ratio of dissociation constants, $K_{D,1}/K_{D,2}$, determines the selectivity of sequence 2 to sequence 1. In Table 2, the selectivity of PT versus MM2a, MM2b, and MM4a is, within error, nonexistent. If both PT and MM2a or MM2b are present in similar concentrations, the assay will not effectively discriminate between the two.

In order to lower the effective dissociation constant as well as shorten the overall assay time, we created a microfluidic platform which relies on ion concentration polarization by a cation-exchange membrane and aggregation of DNA-linked nanoparticles in gel. In this design, a DNA target links together nanoparticles functionalized with two different complementary probes into dimers, trimers, and higher multimers. After insertion into the chip (Fig. 1A), electrophoresis drives the sample of gold particles and DNA towards the membrane where electrostatic repulsion prevents the analytes from passing through. Instead, they concentrate at the membrane surface as in Fig. 1B. In the second step, depletion, we reverse the field to separate the unlinked particles from the linked particles possessing captured target molecules. The membrane prevents anions on the reservoir side from passing through to the channel side while anions on the channel side migrate away from the membrane. Furthermore, the electroneutrality constraint prevents cations on the channel side from migrating past the anions despite being driven

towards the membrane by the electric field. Consequently, a region depleted of ions forms beneath the membrane and progresses up the channel towards the sample reservoir. The interface between this depletion region and the concentrated ion front creates a steep conductivity gradient in which the faster moving monomers, that is, the unlinked particles, separate from the slower moving multimers, the linked particles, based on the difference in their electrophoretic mobilities. The depletion region eventually overtakes the particles, and the high electric field induces aggregation of the linked particles. In Fig. 1C, there is a clear separation of the monomers and the aggregates. The multimers aggregate preferably over the monomers for two reasons. One is the cation condensation around the DNA duplexes lowers the barrier to aggregation. The second reason is the duplexes also tether multiple particles together thereby keeping two or more particles within range of the attractive van der Waals forces [24]. Subsequently, the aggregates become too large to pass through the pores of the gel and immobilize.

As reported in our previous work [24], we use this technique to achieve a limit of detection down to 10 pM DNA, or about ten million copies. We can also examine the dissociation constant to determine the improvement in our chip-based assay with ion concentration polarization over solution-phase or other assays which possess no preconcentration capabilities. In surface-based hybridization assays, the dissociation constant indicates the initial target concentration required to bind 50% of the probes. Since it is difficult to accurately quantify the exact amount of probe-target hybridization in our chip assay, we approximate an effective dissociation constant, $K_{D,eff}$, at which fifty percent of our nanoparticles aggregate. From our calibration data, we report $K_{D,eff}$ of 1 nM. We can lower $K_{D,eff}$ even further by extending the enrichment time. For instance, for 10 min of enrichment we can lower this value to below 500 pM; this is a nearly 100-fold improvement over the equilibrium-based assay which has a dissociation constant of only 50 nM as shown in Table 2. The primary reason for this improvement is the concentration of probes, targets, and cations at the membrane during the enrichment step which drives the hybridization reaction in the forward direction. The aggregation during the depletion step prevents the reverse reaction from occurring and therefore maintains the enrichment effect.

While the enrichment effect suitably enhances the limit of detection for target molecules, the effect is also pertinent to undesirable nontargets. When the dissociation constant of the nontarget is sufficiently different from that of the target, selectivity is not an issue as we demonstrated in our previous work [24]. When the hybridization free energies share a difference of only a couple kilojoules per mole, such as the sequences in Table 2, then distinguishing targets from mismatches becomes virtually impossible. The similarity in dissociation constants guarantees mismatches will report a false positive signal if they are present within the sample.

To overcome this clear drawback, we altered our protocol to take advantage of differences in the rates of dehybridization between mismatches and targets as opposed to differences in

the magnitudes of the dissociation constants. In short, we used electric field ramping to alter the final amount of hybridized targets or mismatches. We began by examining how the strength of the electric field during the depletion step affected the fraction of aggregation. After initially applying the field at 200 V for 1 min, we dropped the field to various voltages for the remainder of the depletion step. As shown in Fig. 4 of our previous work [24], the ratio of target intensity to mismatch intensity decreases at higher voltages because there is substantial dehybridization by both targets and mismatches. However, when ramped to a low enough voltage at 125 or 100 V, the particles retain the target DNA while expelling most of the mismatch DNA. To enhance this effect further, we explored the effect of changing the amount of time used for the initial depletion potential. The reason for starting at such a high potential is to quickly initiate the onset of the depletion zone and increase the electrical shear force on the particles. As the depletion zone spreads away from the membrane, there is a sharp rise in the electric field. This generates a strong electric shearing force which contributes to the dehybridization of targets and mismatches. The longer this strong shear force is active, i.e. during the application of the 200 V, the more dehybridization should occur. However, if active too long, both targets dehybridize nonselectively. When we lower the depletion potential, we still enable dehybridization but at a slower rate. Furthermore, as the depletion zone grows up the channel, the electric field will drop as the high resistance region increases in length. In addition, we believe the accompanying drop in current indicates Joule heating does not play a significant role in enhancing dehybridization. In the supplementary information of our previous manuscript, we recorded the current during

the depletion step [24]. The current is relatively low (< 1 mA) and continues to fall proportional to the square root of time. Furthermore, the agarose gel and the high surface area to volume ratio of the microchannel provide good heat dissipation. Hence, we attribute dehybridization effects primarily to the electric field.

Our results are shown in Fig. 3. Here, the x-axis represents the amount of time we apply our high electric shear force using the 200 V depletion potential before ramping this potential down to 125 V for the remainder of the depletion step. For example, time t = 1 min indicates we hold the voltage at 200 V for one minute before making a step change down to 125 V. At time t = 0 then, we simply begin the depletion voltage at 125 V with no change for the duration of the depletion step. We compare the fraction of aggregation remaining for the perfectly matched target, targets with two and four mismatches at the end of the pairing sequence, and targets with two and four mismatches in the middle of the pairing sequence. Here, we subtract the baseline aggregation amount in order to accurately compare the selectivity between PT and the other sequences. Figure 3 shows there is indeed a clear trend in which longer shear times lead to better selectivity. The rate at which the selectivity improves with increasing shear times is dependent on the location as well as the number of mismatches. For instance, there is complete selectivity of PT to all other sequences at 1 min. As we go from 1 min to 0.5 min and 0 min, the selectivity ratio decreases for both MM2a and MM2b but slightly faster for MM2b where the mismatch in the middle. For MM4a and MM4b, the signal is insignificant until 0 min. Again, the selectivity is slightly better against MM4a although this difference is within error of the confidence intervals. The differences demonstrated here validate the importance of mismatch location in determining selectivity as reported in previous work by our group [39]. In the prior work, mismatches placed within the middle of the pairing sequence significantly increased the difficulty of differentiating the mismatch from the target sequence. Changing the mismatch location from the end of the sequence to the middle of the sequence reduced the selectivity from greater than 75 to only 1.5. Figure 3 displays a different trend where end mismatches provide inferior selectivity to middle mismatches. However, in our case we can still distinguish both middle and end mismatches from target. In addition, doubling the number of mismatches from two to four significantly improves the selectivity, and this is true for both the middle and end mismatches. The selectivity here is a substantial improvement when compared to the selectivity provided by the ratio of dissociation constants. In the case of an equilibrium assay, when dissociation constants are the determining factors, the PT and MM2a sequences are impossible to distinguish as shown by Table 2. The selectivity we report for our platform is superior to the values of two to six for previously reported assays which rely on probe-functionalized nanoparticles [28, 29]. Importantly in our assay, we clearly demonstrate an improvement in selectivity beyond the equilibrium value. No such data were available to make a similar claim for the cited references.
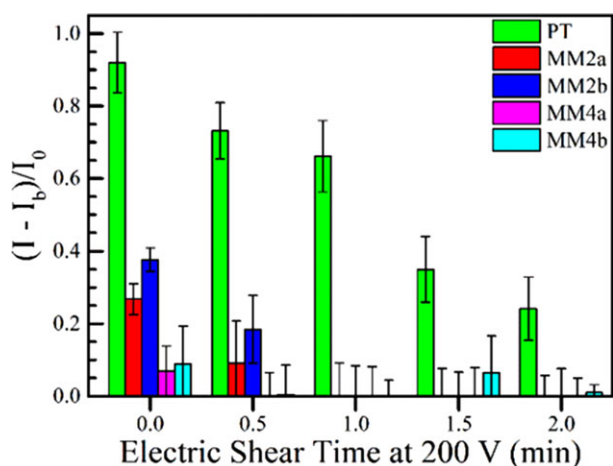

Figure 3. Selectivity improvements obtained by voltage ramping during depletion isotachophoresis. During depletion, the potential was applied at 200 V for various times (electric shear time) before ramping down to 125 V. I_0 is the initial particle intensity after enrichment, I_b is the baseline aggregation (when no DNA is present), and I is the signal intensity for 10 nM DNA. Error bars represent uncertainties within 95% confidence intervals and sample size $n = 4$.
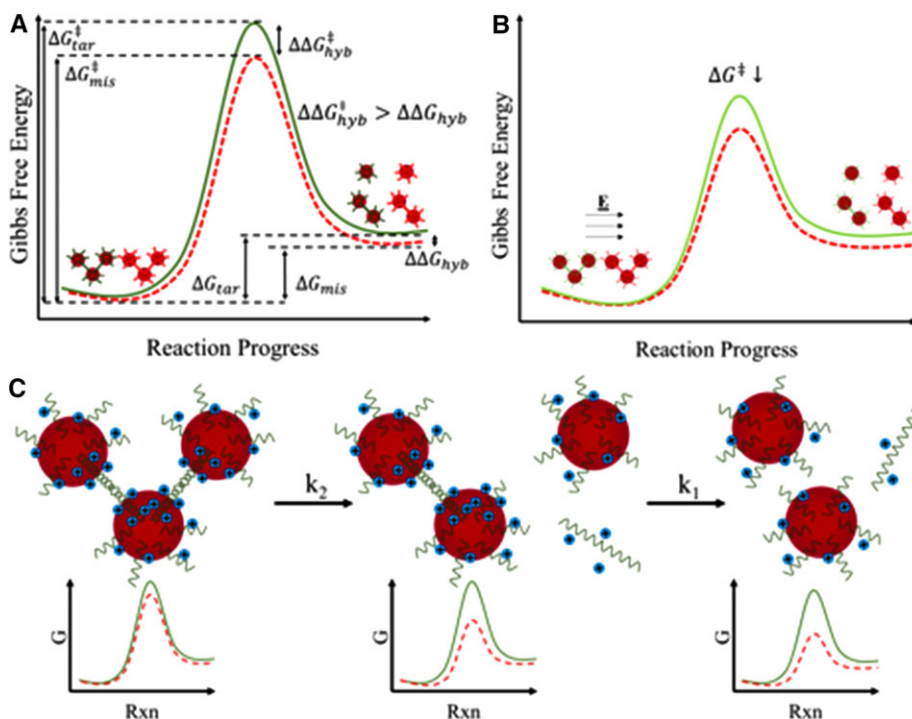
Figure 4. Reaction coordinate diagrams for dehybridization for targets (green solid line) and mismatches (red dashed line). (A) Duplexes face a significant energy barrier to dehybridization. (B) Force from applied electric field destabilizes duplexes thereby raising initial energy and lowering $\Delta G^{\ddagger}$. (In the gel medium, electrical force on each nanoparticle of the duplex is often unequal due to field shielding and physical immobilization of one particle. Hence, the stretching force on the duplex should increase with electric field to destabilize it.) (C) Cooperative melting lowers energy barrier with each successive dehybridization such that $k_1 > k_2$.

4 Discussion

We developed our microfluidic platform as a kinetic answer to a thermodynamic problem. Many electrochemical and colorimetric approaches to sensing rely on equilibrium-based assays. In general, there are three main problems with this approach. One obvious problem is it takes hours or more often days of waiting to reach equilibrium which will significantly slow down throughput. Second, the detection and capture moieties, such as ssDNA probes or antibodies (in the case of proteins), may have relatively high dissociation constants. This restricts the limit of detection to concentrations above the desired range, and it results in poor sensitivity. Finally, the dissociation constants between targets and mismatches are usually very similar thus leading to poor selectivity and false positive signals.

We addressed the first two problems in our previous work [24] through preconcentration of analytes at a cation-exchange membrane. This enrichment step favorably affects the hybridization process by forcing the reaction in the forward direction. The concentration of the target DNA and buffer cations into a small volume at the membrane surface creates an effective dissociation constant nearly two orders of magnitude lower than that provided by equilibrium. The aggregation of the gold nanoparticles during the depletion step ensures favoring the forward reaction is irreversible despite the low cation concentration by preventing any further dehybridization since the hybridized pairs are trapped in the aggregate. Finally, since the preconcentration is driven by electrokinetics, the time required for the assay reduces from days to minutes.

Although the detection of target DNA benefitted from enrichment at the ion-exchange membrane, the major drawback of this approach is it equally enriches undesirable nontarget DNA. While nontargets with a high number of mismatches pose no serious concerns, nontargets with only a few mismatches are virtually indistinguishable from perfectly matched targets. As we revealed in Table 2, this is due to the fact that the targets and mismatches bear almost identical dissociation constants for hybridization to probe-functionalized nanoparticles. Our kinetic solution to this thermodynamic problem was to take advantage of the strong electric field generated during the depletion step to utilize larger differences in dehybridization rates. We illustrate this concept in the reaction coordinate diagrams in Fig. 4A. The difference in the thermodynamic Gibbs free energy for hybridization $\Delta\Delta G_{hyb} = \Delta G_{hyb,tar} - \Delta G_{hyb,mis}$ is typically just a few RT for two mismatches giving rise to very little thermodynamic equilibrium selectivity as shown by Eq. (3):

$$\frac{K_{D,mis}}{K_{D,tar}} = e^{-\Delta\Delta G_{hyb}/RT} \tag{3}$$

However, when we use depletion isotachophoresis, we consider the kinetics of the dehybridization where $\Delta\Delta G^{\ddagger}_{d} = \Delta G^{\ddagger}_{d,tar} - \Delta G^{\ddagger}_{d,mis}$ is the controlling factor. In the presence of shear, both targets and mismatches will dehybridize irreversibly, but they will dehybridize at different rates. The shearing force destabilizes the duplex thereby raising its energy and reducing the energy barrier, $\Delta G^{\ddagger}_{d}$. For a first order reaction, the relative change in concentration, C/C_0, over time, t, with a rate constant, k_d, is given by

$$\frac{C}{C_0} = e^{-k_d t} \tag{4}$$

Therefore, given similar initial concentrations, the selectivity will be

$$\frac{C_{tar}}{C_{mis}} = e^{-(k_{d,tar} - k_{d,mis})t} \tag{5}$$

If we substitute in the definitions of the rate constants, Eq. (6) reduces to

$$\frac{C_{tar}}{C_{mis}} = \exp\left[-k_{d,tar} t \left(1 - \frac{k_{0,mis}}{k_{0,tar}} e^{\frac{\Delta\Delta G_d^{\ddagger}}{RT}} \right) \right] \tag{6}$$

where $k_{0,tar}$ and $k_{0,mis}$ are the preexponential factors. To ensure that the target concentration does not decrease appreciably to compromise the sensitivity, irreversible dehybridization is stopped after some time that is not much larger than $1/k_{d,tar}$. At that time, the selectivity is controlled by the double exponential of $\Delta\Delta G_d^{\ddagger}$ which is larger than the single exponential of ΔG_{hyb} at equilibrium, even if both quantities are comparable. The difference becomes exponentially large when the barrier difference is much larger than RT. Therefore, unless the preexponential factors for the kinetic constants are very different for the two molecules, due perhaps to entropic effects introduced by the mismatches, the kinetically controlled selectivity is expected to be exponentially (geometrically) better than thermodynamic equilibrium selectivity for barrier differences much larger than RT. Sedighi et al. [28] measured $\Delta\Delta G_d^{\ddagger}$ for their NanoBioArray chip which also uses DNA hybridization to DNA-functionalized gold nanoparticles. They compared the dehybridization activation free energies for a perfectly matched target and one-base mismatch with twenty-base pairing sequences on 12 nm gold nanoparticles. According to their results, $\Delta\Delta G_d^{\ddagger}$ was −2.7 kJ/mol. From our data in Table 2, a two-base mismatch yields a $\Delta\Delta G_{hyb}$ of 1 kJ/mol or less if we consider the level of uncertainty. Since $\Delta\Delta G_d^{\ddagger}$ and $\Delta\Delta G_{hyb}$ are both on the order of 1 kJ/mol, the quantities are indeed comparable. Therefore, we should expect the kinetic paradigm of dehybridization to facilitate better selectivity than thermodynamic equilibrium.

It is also clear from this analysis that there is a tradeoff between selectivity and signal intensity. We see this by examining the limits of the target concentration and the selectivity as time goes to infinity. From Eq. (4), the concentration of target approaches zero as time goes to infinity. From Eq. (5), however, since $k_{d,mis}$ is greater than $k_{d,tar}$, the selectivity approaches infinity as time goes to infinity. While selectivity increases with increasing shear time, a loss in signal intensity due to target dehybridization always accompanies it. We see this effect in Fig. 3 where the selectivity increases with increasing shear time, but the amount of aggregation for target steadily decreases. Our goal, therefore, is to maximize the rate at which selectivity approaches infinity while simultaneously minimizing the rate at which the target concentration approaches zero. Furthermore, this must occur before inducing particle aggregation. To achieve this, we turn to cooperative melting.

We propose cooperative melting further enhances this selectivity by irreversible kinetics allowing us to retain a higher concentration of target than by shear alone. As explained above, cooperative melting describes how hybridization or dehybridization of one target favorably or unfavorably contributes to further hybridization or dehybridization events. In our case, we concern ourselves with the effect of positive cooperativity on dehybridization. According to Lei et al., positive cooperativity occurs when the surface probe density is between approximately 0.04 and 0.10 oligos per nm^2 and when the salt concentration is greater than 0.2 M [43]. Based on previous reports [16, 46], we expect the surface probe density on our particles to be about 0.08 oligos per nm^2. Our $1 \times$ TAE buffer is 40 mM tris-acetate which easily concentrates more than ten-fold during the enrichment portion of our assay. Therefore, we should be in the positive cooperativity region during the initial stages of our depletion step. In this regime, successive dehybridization events are energetically more likely to accompany a reduction in the kinetic energy barrier thereby accelerating the reaction. The reason for acceleration is the association of cations around DNA duplexes. When the targets hybridize to their probes, they require a larger number of cations than either targets or probes alone in order to compensate for the increased charge density [47]. The increased density of cations around the duplexes on the gold nanoparticles provides a stabilizing effect for additional hybridization. Consequently, when targets dehybridize from the nanoparticle probes, they diminish the cation concentration which destabilizes the remaining duplexes making dehybridization of the next target energetically more favorable than the previous one.

The positive cooperativity expressed here proves to be highly advantageous for improving the selectivity between targets and mismatches. In essence, cooperativity implies that dehybridization is not one single reaction but rather a series of successive reactions which all possess their own rate constant. If there are N targets bound to each nanoparticle, and the rate constant for each dehybridization is k_N, then $k_N < k_{N-1} < k_{N-2} \ldots$. In other words, the reaction is self-accelerating. Because mismatches already have a lower rate constant than targets, their dehybridization accelerates at a faster rate than the targets'. In fact, the rate of dehybridization for mismatches can be sped up even more relative to target dehybridization by optimally timing the voltage ramping. After sufficiently accelerating the dehybridization of mismatches, decreasing the electric field at the optimal time allows us to retain the targets by slowing down their dehybridization. Although the rate of mismatch dehybridization also slows, the initial acceleration provides enough of an impetus to increase the rate well beyond the rate of the target. We therefore maximize the retention of targets and minimize the number of mismatches thus increasing the signal intensity while avoiding false positives. This effect is partially obscured by the fact that dehybridization essentially ends once the particles aggregate which is dependent on the growth of the depletion region. The rate of dehybridization and depletion are both dependent on the strength of the electric field, so determining the exact rate of dehybridization remains a complex set of interactions.

Cooperative melting may also explain the discrepancy between this work and our previous work [39] as to the effect of mismatch location. Normally, we expect there to be greater selectivity when mismatches are at the end of the DNA sequence because duplexes dehybridize through an unzipping mechanism whereby the base pairs break their bonds at one end of the sequence continuing down to the opposite end [48]. In our case, the middle mismatches in MM2a are near the particle surface whereas the end mismatches in MM2b lie at the opposite end. Near the particle surface is where cooperative melting effects the biggest changes in charge density. It could therefore lower the kinetic barrier to melting for MM2a more so than for MM2a, and this may account for the slightly better selectivity against MM2a. We also note that in the previously cited work, probe DNA was functionalized on 500 nm silica nanocolloids. Hill et al. pointed out that the behavior of DNA hybridization to surface-functionalized probes on nanoparticles approaches that of hybridization to probes on planar surfaces when the diameter of the nanoparticles is above 60 nm [16]. Hence, the cooperative melting effect is likely to be more pronounced for our present nanoparticle assay than in our previously reported nanocolloid assembly.

Our microfluidic platform for detecting short nucleic acids used depletion isotachophoresis and gold nanoparticle aggregation to improve the limit of detection and sensitivity, decrease the time required for detection, and increase the selectivity compared to conventional equilibrium assays. Preconcentration of reagents through ion concentration polarization reduces the effective dissociation constant down to 500 pM. Our assay requires fifteen minutes from sample insertion to quantification and only a 2 μL sample volume. Conventional equilibrium assays such as microarrays or lateral flow, which rely on diffusion to surface-based probes, possess poor sensitivity and little selectivity in comparison. Current nanoparticle hybridization assays feature selectivities less than ten because they do not incorporate shear forces [28, 29]. The critical feature increasing the selectivity is the voltage ramping during the depletion step. The high electric field during this step provided substantial energy to dehybridize targets or mismatches on a timescale of seconds. The thermodynamic parameters revealed by the melting curve experiments demonstrated an equilibrium assay was unsuitable to achieve good selectivity between DNA targets and mismatches. Dehybridization caused by the depletion step, however, made the selectivity kinetically controlled and led to significant improvements. Kinetic control should yield exponentially greater selectivity than thermodynamic control because of irreversibility due to shear, when $\Delta\Delta G^{\ddagger}_{d}$ is much larger than RT. Cooperative melting and optimal timing of the voltage ramping enhanced the selectivity even further. One key to this assay is the irreversibility of the dehybridization reaction. Mismatches which dissociate during the depletion step are swept away by the electric field and prevented from rehybridizing with the probes. In essence, there is an insurmountable energy barrier which prevents the mismatches from rehybridizing despite the thermodynamic

favorability of the duplex state. Finally, previous studies examined the conditions under which positive cooperativity is highly favorable such as high salt concentration and moderate surface probe densities. Preparing oligo-functionalized nanoparticles in this range will enable them to deliver superior selectivity.

The authors have declared no conflict of interest.

5 References

[1] Wang, F., Zheng, Z., Guo, J., Ding, X. *Gynecol. Oncol.* 2010, *119*, 586–593.

[2] Zhi, F., Chen, X., Wang, S., Xia, X., Shi, Y., Guan, W., Shao, N., Qu, H., Yang, C., Zhang, Y., Wang, Q., Wang, R., Zen, K., Zhang, C. Y., Zhang, J., Yang, Y. *Eur. J. Cancer.* 2010, *46*, 1640–1649.

[3] De Smaele, E., Ferretti, E., Gulino, A. *Brain Res.* 2010, *1338*, 100–111.

[4] Hummel, R., Hussey, D. J., Haier, J. *Eur. J. Cancer.* 2010, 298–311.

[5] Woolley, A. T. *Anal. Bioanal. Chem.* 2015, (Jun 2015).

[6] Brunet-Vega, A., Pericay, C., Quilez, M. E., Ramirez-Lazaro, M. J., Calvet, X., Lario, S., *Anal. Biochem.* 2015, *488*, 28–35.

[7] Dong, H., Lei, J., Ding, L., Wen, Y., Ju, H., Zhang, X. *Chem. Rev.* 2013, *113*, 6207–6233.

[8] Pritchard, C. C., Cheng, H. H., Tewari, M. *Nature Rev.* 2012, *13*, 358–369.

[9] Qu, Y., Marshall, L. A., Santiago, J. G. *Anal. Chem.*, 2014, *86* 7264–7268.

[10] Lekchnov, E. A., Zaporozhchenko, I. A., Morozkin, E. S, Bryzgunova, O. E., Vlassov, V. V., Laktionov, P. P. *Anal. Biochem.* 2016, *499*, 78–84.

[11] Xu, J., Craig, S. L. *J. Am. Chem. Soc.* 2005, *127*, 13227–13231.

[12] Fiche, J. B., Buhot, A., Calemczuk, R., Livache, T. *Biophys. J.* 2007, *92*, 935–946.

[13] Lytton-Jean, A. K. R., Mirkin, C. A. *J. Am. Chem. Soc.* 2005, *127*, 12754–12755.

[14] Jin, R., Wu, G., Li, Z., Mirkin, C. A., Schatz, G. C. *J. Am. Chem. Soc.* 2003, *125*, 1643–1654.

[15] Ravan, H., Kashanian, S., Sanadgol, N., Badoei-Dalfard, A., Karami, Z. *Anal. Biochem.* 2014, 41–46.

[16] Hill, H. D., Millstone, J. E., Banholzer, M. J., Mirkin, C. A. *ACS Nano.* 2009, *3*, 418–424.

[17] Ko, S. H., Song, Y. A., Kim, S. J., Kim, M., Han, J., Kang, K. H. *Lab Chip.* 2012, *12*, 4472–4482.

[18] Lee, J. H., Chung, S., Kim, S. J., Han, J. *Anal. Chem.* 2007, *79*, 6868–6873.

[19] Kim, S. J., Li, L. D., Han, J. *Langmuir.* 2009, *25*, 7759–7765.

[20] Wang, Y. C., Stevens, A. L., Han, J. *Anal. Chem.* 2005, *77*, 4293–4299.

[21] Quist, J., Janssen, K. G. H., Vulto, P., Hankemeier, T. van der Linden, H., *J. Anal. Chem.* 2011, *83*, 7910–7915.

[22] Quist, J., Vulto, P., van der Linden, H., Hankemeier, T. *Anal. Chem.* 2012, *84*, 9065–9071.

[23] Slouka, Z., Senapati, S., Chang, H. C. *Annu. Rev. Anal. Chem.* 2014, *7*, 317–335.

[24] Marczak, S., Senapati, S., Slouka, Z., Chang, H.-C. *Biosens. Bioelectron.* 2016, *86*, 840–848.

[25] de Avila, B. E. F., Watkins, H. M., Pingarron, J. M., Plaxco, K. W., Palleschi, G. P., Ricci, F. *Anal. Chem. 85*, 6593–6597 (2013).

[26] Graybill, R. M., Bailey, R. C. *Anal. Chem.* 2016, *88*, 431–450.

[27] Fuchs, R. T., Sun, Z., Zhuang, F., Robb, G. B. *PLOS One.* 2015, *10*, e0126049.

[28] Sedighi, A., Li, P. C. H., Pekcevik, I. C., Gates, B. D. *ACS Nano*, *8*, 6765–6777 (2014).

[29] Cao, Q., Teng, Y., Yang, X., Wang, J., Wang, E., *Biosens. Bioelectron.* 2015, *74*, 318–321.

[30] Luo, X. W., Du, F. J., Wu, Y., Gao, L. J., Li, X. X. *Chin. J. Anal. Chem.* 2013, *41*, 1664–1668.

[31] Jia, L., Shi, S., Ma, R., Jia, W., Wang, H. *Biosens. Bioelectron.* 2016, *80*, 392–397.

[32] Li, Z., Miao, X., Xing, K., Zhu, A., Ling, L. *Biosens. Bioelectron.*, 2015, *74*, 687–690.

[33] Noor, M. O., Krull, U. J. *Anal. Chim. Acta.* 2011, *708*, 1–10.

[34] Pan, H. Z., Yu, H.W., Wang, N., Zhang, Z., Wan, G. C., Liu, H., Guan, X., Chang, D. *J. Biotech.* 2015, *214*, 133–138.

[35] Noor, M. O., Tavares, A. J., Krull, U. J. *Anal. Chim. Acta*, 2013, *788*, 148–157.

[36] Garcia-Schwarz, G., Santiago, J. G. *Anal. Chem.* 2012, *84*, 6366–6369.

[37] Bercovici, M., Han, C. M, Liao, J. C., Santiago, J. G. *PNAS.* 2012, *109*, 11127–11132.

[38] Sosnowski, R. G., Tu, E., Butler, W. F., O'Connell, J. P., Heller, M. J. *PNAS.* 1997, *94*, 1119–1123.

[39] Cheng, I. F., Senapati, S., Cheng, X., Basuray, S., Chang, H. C., Chang, H.-C. *Lab Chip.* 2010, *10*, 828–831.

[40] Cheng, I. F., Han, H. W., Chang, H.-C. *Biosens. Bioelectron.* 2012, *33*, 36–43.

[41] Heaton, R. J., Peterson, A. W., Georgiadis, R. M. *PNAS.* 2001, *98*, 3701–3704.

[42] Ali, M. F., Kirby, R., Goodey, A. P., Rodriguez, M. D., Ellington, A. D., Neikirk, D. P., McDevitt, J. T. *Anal. Chem.* 2003, *75*, 4732–4739.

[43] Lei, Q. L., Ren, C. L., Su, X. H., Ma, Y. Q. *Sci. Rep.* 2015, *5*, 9217.

[44] Lytton-Jean, A. K. R., Gibbs-Davis, J. M., Long, H., Schatz, G. C., Mirkin, C. A., Nguyen, S. T. *Adv. Mat.* 2009, *21*, 706–709.

[45] Turner, D. H., SantaLucia, J. *Biopoly.* 1997, *44*, 309–319.

[46] Demers, L. M., Mirkin, C. A., Mucic, R. C., Reynolds, R. A., Letsinger, R. L., Elghanian, R., Viswanadham, G. *Anal. Chem.* 2000, *72*, 5535–5541.

[47] Gong, P., Levicky, P. *PNAS.* 2008, *105*, 5301–5306.

[48] Volkov, S. N., Solov'yov, A. V. *Eur. Phys. J. D.* 2009, *54*, 657–666.